JPhys Energy

PAPER • OPEN ACCESS

Back and front contacts in kesterite solar cells: state-of-the-art and open questions

To cite this article: Charlotte Platzer-Björkman *et al* 2019 *J. Phys. Energy* **1** 044005

View the article online for updates and enhancements.

Recent citations

- Fabrication of monolithic CZTS/Si tandem cells by development of the intermediate connection
Matteo Valentini *et al*

This content was downloaded from IP address 130.238.22.129 on 02/10/2019 at 08:18

JPhys Energy

PAPER

Back and front contacts in kesterite solar cells: state-of-the-art and open questions

Charlotte Platzer-Björkman[1], **Nicolas Barreau**[2], **Marcus Bär**[3,4,5,6], **Leo Choubrac**[7], **Louis Grenet**[8,9], **Jaeyeong Heo**[10], **Tomas Kubart**[1], **Alberto Mittiga**[11], **Yudania Sanchez**[12], **Jonathan Scragg**[1], **Soumyadeep Sinha**[10] **and Matteo Valentini**[11]

[1] Solid State Electronics, Department of Engineering Sciences, Uppsala University, Uppsala, Sweden
[2] Institut des Matériaux Jean Rouxel (IMN), UMR6502, CNRS, Université de Nantes, Nantes, France
[3] Department of Interface Design, Helmholtz-Zentrum Berlin für Materialien und Energie GmbH (HZB), Berlin, Germany
[4] Energy Materials *In-Situ* Laboratory Berlin (EMIL), Helmholtz-Zentrum Berlin für Materialien und Energie GmbH, Berlin, Germany
[5] Helmholtz-Institute Erlangen-Nürnberg for Renewable Energy (HI ERN), Berlin, Germany
[6] Department of Chemistry and Pharmacy, Friedrich-Alexander-Universität (FAU) Erlangen-Nürnberg, Erlangen, Germany
[7] Department of Structure and Dynamics of Energy Materials, Helmholtz-Zentrum Berlin, Berlin, Germany
[8] CEA, LITEN, Grenoble, France
[9] Univ. Grenoble Alpes, Grenoble, France
[10] Department of Materials Science and Engineering, and Optoelectronics Convergence Research Center, Chonnam National University, Gwangju, Republic of Korea
[11] ENEA Casaccia Research Center, Roma, Italy
[12] Catalonia Institute for Energy Research (IREC), Barcelona, Spain

E-mail: charlotte.platzer@angstrom.uu.se

Keywords: thin film solar cells, kesterite, back contact, front contact, buffer layer

OPEN ACCESS

RECEIVED
29 March 2019

REVISED
17 July 2019

ACCEPTED FOR PUBLICATION
30 July 2019

PUBLISHED
1 October 2019

Original content from this work may be used under the terms of the Creative Commons Attribution 3.0 licence.

Any further distribution of this work must maintain attribution to the author(s) and the title of the work, journal citation and DOI.

Abstract

We review the present state-of-the-art within back and front contacts in kesterite thin film solar cells, as well as the current challenges. At the back contact, molybdenum (Mo) is generally used, and thick $Mo(S, Se)_2$ films of up to several hundred nanometers are seen in record devices, in particular for selenium-rich kesterite. The electrical properties of $Mo(S, Se)_2$ can vary strongly depending on orientation and indiffusion of elements from the device stack, and there are indications that the back contact properties are less ideal in the sulfide as compared to the selenide case. However, the electronic interface structure of this contact is generally not well-studied and thus poorly understood, and more measurements are needed for a conclusive statement. Transparent back contacts is a relatively new topic attracting attention as crucial component in bifacial and multijunction solar cells. Front illuminated efficiencies of up to 6% have so far been achieved by adding interlayers that are not always fully transparent. For the front contact, a favorable energy level alignment at the kesterite/CdS interface can be confirmed for kesterite absorbers with an intermediate [S]/([S]+[Se]) composition. This agrees with the fact that kesterite absorbers of this composition reach highest efficiencies when CdS buffer layers are employed, while alternative buffer materials with larger band gap, such as $Cd_{1-x}Zn_xS$ or $Zn_{1-x}Sn_xO_y$, result in higher efficiencies than devices with CdS buffers when sulfur-rich kesterite absorbers are used. Etching of the kesterite absorber surface, and annealing in air or inert atmosphere before or after buffer layer deposition, has shown strong impact on device performance. Heterojunction annealing to promote interdiffusion was used for the highest performing sulfide kesterite device and air-annealing was reported important for selenium-rich record solar cells.

1. Introduction

Kesterite solar cells, i.e. thin film solar cells (TFSCs) based on $Cu_2ZnSn(S, Se)_4$ (CZTSSe) are interesting since they combine the benefits of thin film technology with the use of earth-abundant and non-toxic elements (or low toxic in the case of Se) in photovoltaics. The high absorption coefficient and ideal band gap energy of Se-free

© 2019 The Author(s). Published by IOP Publishing Ltd

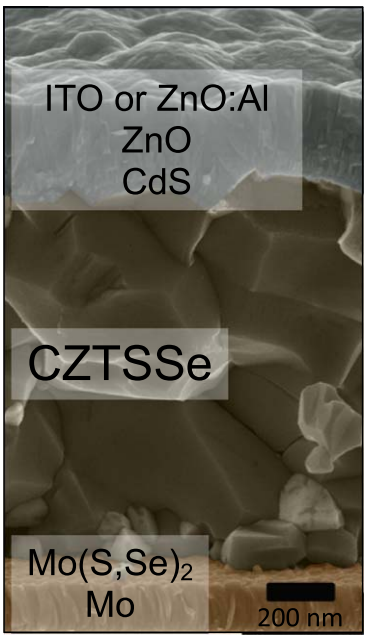

Figure 1. Scanning electron micrograph cross section of a kesterite-based solar cell device stack, courtesy of T Ericson. The Mo back contact usually reacts with S and/or Se present in the absorber formation process step to form a relatively thick $Mo(S, Se)_2$ layer in between Mo and CZTSSe. The kesterite absorber layer is around 1 μm thick for the depicted cell; thicknesses between 600 nm to 2 μm are common. The top contact structure consists, in this case, of 60 nm of CdS, 80 nm of i-ZnO, and a 200 nm thick ZnO:Al layer.

Cu_2ZnSnS_4 (CZTS) absorbers for solar cell applications was first reported by Ito and Nakazawa [1]. Early results on CZTS device performance were reported by Friedlmeier *et al* [2], Seol *et al* [3], and Katagiri *et al* [4]. Later a group at IBM reached record performances with power conversion efficiencies (PCEs) above 10% for CZTSSe devices in 2010 [5] and the current record PCE of 12.6% in 2013 [6]. In 2018, researchers from DGIST reached the same performance, 12.6%, but for a larger device area [7]. The device structure used for kesterite solar cells was originally copied from that of $Cu(In, Ga)Se_2$, (CIGSe) TFSCs, and is formed by sequential deposition, upon a soda lime glass substrate, of a Mo back contact, the absorber, a CdS buffer layer, and a ZnO/ZnO:Al bi-layer window (i.e. transparent top contact). This structure, schematically shown for CZTSSe in figure 1, is not necessarily ideal for kesterite solar cells, and extensive work has been invested into studies of alternative back- and front contacts and related deposition processes. In this paper, the state-of-the-art and current open questions related to the back and front contacts and their respective interfaces are reviewed.

Kesterite TFSCs are similar to the more mature thin film technologies based on CIGS and CdTe absorbers, but so far with lower device efficiency. These three technologies are all composed of absorber/emitter pn-heterojunctions with a total device thickness of only a few micrometers. An advantage compared to CdTe and high efficiency perovskite solar cells is that kesterite solar cells can be made without toxic elements. Kesterite TFSCs have been demonstrated on transparent [8] and flexible substrates [9, 10]. Furthermore, high radiation hardness for space applications has been shown [11]. Some work on long term stability has been reported for kesterite monograin solar cells reaching over 90% of initial efficiency after 3000 h of un-encapsulated dry heat exposure [12], demonstrating good stability of the material. For a thorough coverage of upscaling and reliability of kesterites, we refer to a dedicated paper in this special issue.

There are several requirements that must be met by the contacts in kesterite solar cells. Some requirements are universal for the different compositions, and thereby band gap energies, of the CZTSSe absorbers, and some are specific. In this review, we concentrate on CZTS, S-free kesterite (CZTSe) and CZTSSe absorbers, with some examples where the kesterite material has been alloyed with Ge, Cd, or In. For the back contact, we separate between electronic structure, such as the energy band diagram and electrical properties of $Mo(S, Se)_2$, and chemical properties, such as interdiffusion, reactions of the Mo back contact during absorber deposition, and the effect of interlayers. We also address transparent back contacts—a topic currently attracting attention with regard to bifacial solar cells or multijunction devices.

For the front contact, we review the results published on the energy level alignment at the (so far) standard CZTSSe/CdS heterointerface as a function of absorber composition. In addition, we discuss the transparent conductive oxide (TCO)-based top layer stack and the influence of variations in CdS deposition process and interface treatments that are widely used for higher performance devices. Observations on metastable device behavior for certain window layer stacks or processes are addressed. Finally Cd-free alternative buffer layers are

reviewed, for which the efficiency of corresponding CZTS solar cells is now approaching that of the record devices with CdS buffer, while for CZTSSe and CZTSe, Cd-free buffer layers so far lead to lower efficiencies.

2. The back contact

An overview of device results for some of the different back contacts that have been studied for kesterite TFSCs is given in table 1. The table includes highest reported efficiencies for CZTSSe, CZTSe, and CZTS devices and their reported Mo(S, Se)$_2$ thicknesses, if applicable/reported. Furthermore, the device performance of cells with alternative back contact stacks is presented together with that of their corresponding Mo back contact reference devices, if reported. The sections below address the electronic structure and chemical properties of these contacts. In addition, the results on transparent back contacts are discussed.

2.1. Mechanical properties

A necessary role of the back contact is ensuring adhesion between the CZTSSe absorber and the substrate. Pinhole formation, buckling, bubbling, cracking, or delamination of the overlayer (i.e. the CZTSSe) are some of the various failure mechanisms that can result when mechanical stresses overcome weak physicochemical bonding at an interface [29]. Mechanical stresses can arise for several reasons. First, they can be induced by the deposition methods used for the Mo and CZTSSe layers—techniques such as sputtering, evaporation and electrodeposition, for example, often result in residual stresses in thin films (see [30] for a detailed overview on this topic). Second, a mismatch exists in the thermal expansion coefficients of the absorber and substrate: the linear thermal expansion coefficient of bulk CZTS calculated from data in [31] is about 12 ppm $°C^{-1}$ at 25 °C, compared to about 9 ppm $°C^{-1}$ for the soda-lime glass (SLG) substrate. This will result in development of a certain stress during heating and cooling (for $CuInSe_2$ the same value is about 8–9 ppm $°C^{-1}$ [32], suggesting a less favorable situation for CZTS compared to CI(G)Se). Third, CZTSSe films can exchange material with the gas phase during heating, gaining or losing S(e) and SnS(e). The resulting volume change of the film may induce or relieve stresses depending on the situation. Generalizations cannot be made, but if adhesion problems are experienced, they can potentially be remedied by tuning the stress in the CZTSSe layer via sputter parameters (primarily gas pressure and substrate temperature) [33, 34] or via composition control and if possible, reducing the thickness of the CZTSSe layer [30]. To promote adhesion further, the physicochemical strength of interfaces in general can be improved by enhanced surface roughness and ensuring cleanliness of surfaces prior to deposition [29]. For the CZTSSe back contact in particular, if Mo(S, Se)$_2$ growth occurs with the *c*-axis perpendicular to the Mo plane, see figure 2, then adhesion is reliant upon the weak van der Waals forces that hold the Mo(S,Se)$_2$ sheets together. Thus, this preferred orientation ought to be avoided if interfacial stresses are a problem.

2.2. Chemical properties of the back contact

The back contact is responsible for mediating chemical processes that can have both positive and negative effects on the quality of the solar cell. In this section, we briefly review the ongoing research topics in this area, highlight some relevant materials chemistry aspects, and identify, where possible, gaps in our knowledge that could hold the key to further progress.

2.2.1. Diffusion in thin polycrystalline films

The important chemical processes at the back contact are mediated by *diffusion* of material into or through the back contact layer(s). Diffusion is the net flux of atoms or ions *i* through a given medium *h*, in response to a gradient in the concentration c_i with distance, x (or 'depth' in our case). The flux $J_{i,h}$ is expressed in the 1D case by the law $J_{i,h} = -D_{i,h}\,[\partial c_i/\partial x]$. The diffusion coefficient or 'diffusivity' $D_{i,h}$ describes the rate of hopping of atoms between sites in the crystal, which is thermally activated and thus exponentially dependent on temperature. In perfect solids, the values of $D_{i,h}$ are often very low. However, they become strongly enhanced by the presence of point and extended defects of all kinds. In thin films, grain boundaries (GB) tend to provide the most rapid means of diffusive transport into and through a layer [35]. Given the typical microstructure of magnetron-sputtered Mo back contacts (see figure 1), the relevance of this is obvious.

2.2.2. Diffusion from the substrate

The beneficial diffusion of alkalis (primarily Na) from the SLG substrate through the standard Mo back contact has been well-studied, initially in the case of the related CIGSe materials (e.g. [36, 37]), and there is no reason to suspect any difference for the CZTSSe case. Rapid Na diffusion is observed through Mo thin films, due to the presence of many GB [37]. For Na in particular, Mo-oxides at GB are thought to provide an especially effective diffusion channel (see [36] and references therein), explaining why the diffusion rate of Na is increased with the

Table 1. Device results (total area PCE, open circuit voltage [V_{OC}], short circuit current density [J_{SC}], and fill factor [FF]) for different back contact materials and stacks. The table includes record and high efficiency devices with standard Mo back contact and alternative contacts compared to the standard Mo back contact ('Mo ref'), if data is available. Data is given for CZTSSe, CZTSe, and CZTS based devices with or without anti reflective coating (ARC). The stated band gap energies (E_g) are derived from quantum efficiency measurements reported in the respective references. In cases in which not all information was given in the cited sources, the cells in the table are intentionally left blank.

Back contact stack	Mo(S, Se)$_X$ thickness (nm)	CZTSSe E_g (eV)	V_{OC} (mV)	FF (%)	J_{SC} (mA cm^{-2})	PCE (%)	ARC	Area (cm^2)	References
			CZTSSe						
			541	65.9	35.4	12.6	Yes	0.48	[7]
Mo	≈100	1.13	513	69.8	35.2	12.6	Yes	0.42	[6]
MoO_3/Au			465	60.1	38	10.6		0.04	[13]
Mo ref			358	54.8	32	8.0			[13]
Se/MoO_3/Au		1.1	467	69	36	12.2		0.04	[14]
Mo ref			462	58	31.5	8.4	No		[14]
W		1.03	330	38	30.2	3.8	No	0.25	[15]
Au		1.03	260	43	31.5	3.5	No	0.25	[15]
Mo		1.03	350	44	28.6	4.4	No	0.25	[15]
Mo/TiN	0		365	50	27.5	5	No	0.24	[16]
Mo/TiN/Mo	≈400		439	55	29.5	7.1	No	0.24	[16]
Mo ref	≈1000		436	51	27.6	6.4	No	0.24	[16]
FTO/Mo:Na	≈40	1.09	419	57.2	28.2	6.8	No	0.09	[8]
FTO	0	1.09	314	42.3	19.4	2.6	No	0.09	[8]
			CZTSe						
Mo		1.07	432	76.2	36.3	11.95	No	0.52	[17]
Mo	≈200	1.05	479	63.8	36.5	11.2	Yes	0.30	[18]
Mo trilayer	≈250	≈1.05	463	66.3	38.3	11.8[a]	Yes	0.52	[19]
Mo	≈200	1.0	423	67.3	40.6	11.6	Yes	0.43	[20]
	≈900	1.03	443	68	38.1	11.4	No	0.36	[21]
Mo/TiN	0	1 eV	401	54.7	40.0	8.8	No		[22]
Mo/TiW	Yes[b]	1 eV	330	48.0	35.0	5.3	No		[23]
Mo ref	Yes	1 eV	365	56.6	36.3	7.5	No		[22]
Mo/MoO_2-stack		1 eV	459	65.9	31.6	9.5	No	0.09	[23]
Mo ref		1 eV	392	56.4	32.7	7.2	No	0.09	[23]
FTO		1 eV	389	42.0	35.0	5.72	No		[24]
ITO		1 eV	359	36.7	31.7	4.12	No		[24]
			CZTS						
Mo	≈200	1.5 eV	731	69.3	21.7	11.0	Yes	0.23	[25]
Mo/Al_2O_3	100		658	65.9	19.8	8.57	Yes	0.45	[26]
Mo ref	300		632	61.1	19.0	7.34	Yes	0.45	[26]
Mo/MoO_{3-x}		1.37 eV, $Cu_2(Zn, Cd)SnS_4$	610	63.8	23.1	8.98	Yes		[27]
Mo ref			525	59.6	18	5.5	No		[27]
ITO		1.47 eV	555	62.6	16.7	5.8	No	0.08	[28]
Mo ref		≈1.5 eV	693	50.3	16.9	5.9	No	0.08	[28]

[a] Active area PCE;

[b] $MoSe_2$ observed below the TiW layer, but thickness not stated in [23].

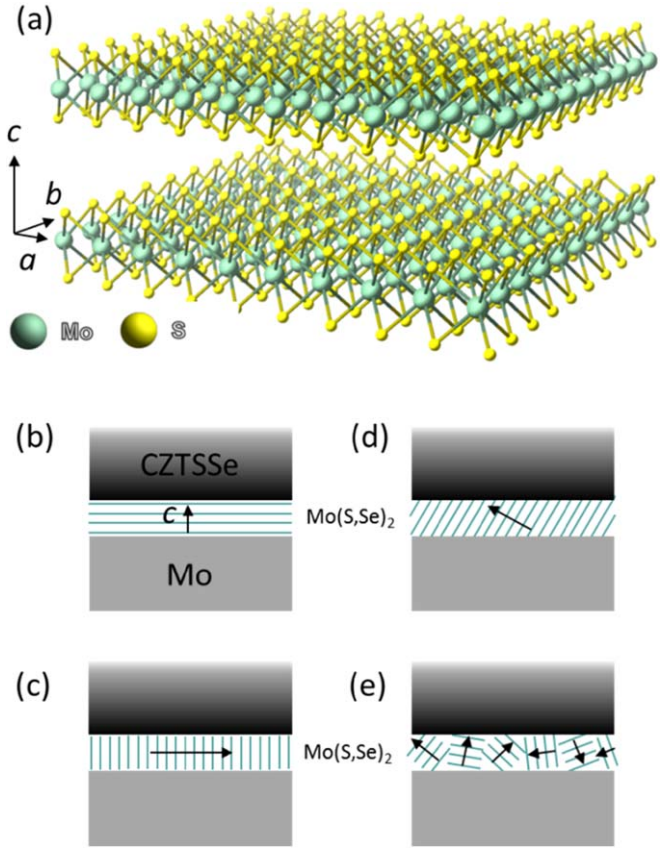

Figure 2. (a): Illustration of the layered crystal structure of $Mo(S, Se)_2$, showing covalently bonded MoS_2 (or $MoSe_2$) layers held together by weak van der Waals forces over a relatively large interlayer gap. (b)–(e) Schematics of possible $Mo(S, Se)_2$ orientations with respect to the solar cell layer structure: *c*-axis oriented perpendicular (b), parallel (c), intermediate (d), or randomly (e) with respect to the substrate surface.

O content in the Mo layer. Therefore, it is possible to tune the diffusivity of Na in the back contact to increase the delivered 'dose' to the absorber layer under the conditions of the chosen thermal process. Apart from the total dose, the lateral *distribution* of Na, both at large and small scales, should ideally be uniform [38]. This puts high demands on the chemical and microstructural uniformity of the back contact layer(s) from nm to mm length scales.

If other substrates besides SLG are used, alkalis must be provided from a separate source [39, 40]. The same is true in the case diffusion barriers on the Mo are used to control the $Mo(S, Se)_2$ thickness. In contrast, any diffusion of detrimental impurities, such as e.g. Fe from a steel substrate, must be avoided. In the case of CIGSe on steel substrates, it has been shown that an additional metal or metal-oxide barrier layer beneath the Mo can have the desired result—see [41] and references therein—and similar results have been reported for CZTSSe [39, 41].

2.2.3. $Mo(S, Se)_2$ growth

Unlike CIGSe, CZTSSe is most often prepared with a large excess of chalcogens in the thermal process, typically 1–1000 mbar in a two stage growth process compared to $\approx 10^{-5}$ mbar for co-evaporation of CIGSe. The formation of a layer of $Mo(S, Se)_2$ is inevitable under such conditions. As discussed in section 2.3 below, factors like the orientation, thickness, and doping of the $Mo(S, Se)_2$ layer can all have significant electrical effects on the solar cell. Here we focus on the effect of the growth environment on the layer properties. The growth rate of the $Mo(S, Se)_2$ layer, assuming a steady supply of chalcogen from the gas phase, ought to be dependent on the rate of diffusion of S(e) through the growing $Mo(S, Se)_2$ layer to reach unreacted Mo [42]. The diffusion rate $J_{S,MoS(e)_2}$ should increase for higher chalcogen partial pressure, due to the enhanced concentration gradient $\partial c_S/\partial x$, and higher temperature via an enhanced diffusivity of S(e) in Mo. However, different groups obtain very thin or thick $Mo(S, Se)_2$ layers for ostensibly similar thermal process conditions, see for e.g. table 1. Part of the explanation may lie in the highly anisotropic nature of $Mo(S, Se)_2$ (see figure 2). Significantly different diffusion coefficients for S(e) can be observed depending on whether the covalently bonded $Mo(S, Se)_2$ sheets are oriented perpendicular to the plane of the back contact (high diffusivity), parallel to it (low diffusivity), with some

intermediate orientation, or with no preferred orientation at all. The angle and degree of orientation obtained in a given process seems to depend on the Mo sputter parameters [43, 44], oxygen content [45, 46], the presence of Na [44], and the conditions of the heat treatment [44]. These factors can all vary from group to group, possibly resulting in a variation of orientations and thus of S(e) diffusivity values and ultimately $Mo(S, Se)_2$ layer thicknesses. Naturally, the diffusivity of Na will be influenced in a similar way, which couples the $Mo(S, Se)_2$ formation process to the CZTSSe absorber properties, and means that if modifications to the back contact are made, other variables may need to be altered to keep the alkali dose in the optimum range. Since the complexity of these interrelated effects could result in trade-offs for device performance, a more attractive approach may be to deposit the $Mo(S, Se)_2$ layer deliberately, instead of allowing it to form in the thermal step. Indeed, it has been shown that MoS_2 can be prepared with controlled orientation using sputtering techniques [47].

As an aside, a direct reaction between CZTS and Mo can be observed when the back contact interface is heated in absence of S, resulting in the decomposition of the CZTS and the formation of MoS_2 [48]. The impact of this process is reduced when high S(e) partial pressures are provided in the thermal step, because the excess S(e) provided can compensate for the chalcogen loss from the absorber layer. Nevertheless, it could become relevant if thermal processes are developed in the future that use lower S(e) partial pressures.

2.2.4. Protective interlayers at the back contact

To protect the back contact from excessive $Mo(S, Se)_2$ formation, the use of interlayers with thicknesses in the sub-100 nm range, placed between the Mo and the CZTSSe, has been tested repeatedly. As reviewed recently by Englund *et al*, interlayers of pure metals as well as various metal borides, carbides, nitrides, and oxides have been deposited between the Mo and CZTS(e) layers for this purpose [49]. In two cases (TiN [16, 50]) the final device efficiency was not improved, but generally an improvement was obtained (TiN [51], Bi [52], Ag [53], C [54], TiB_2 [55], ZnO [56–58], a-SiC [59] , MoO_x [23, 60]). The reported improvements, however, did not result in devices with PCEs higher than 10%, suggesting that to date the $Mo/Mo(S, Se)_2$ layer stack is still the best back contact for CZTSSe solar cells. One exemption might be the application of a 3 nm thick Al_2O_3 interface layer [26]. It reduces the MoS_2 thickness as well as the voids and ZnS segregation at the MoS_2/CZTS interface. This results in an improved time resolved photoluminescence lifetime and in CZTS device performances up to 9.26% (table 1). The same interfacial layer is used in the 11% CZTS record device [25]. Many of these interlayers, especially the metals and oxides, react with S(e) or the CZTSSe layer during processing (e.g. [15, 22]). In some cases, a final top layer of Mo or $Mo(S, Se)_2$ is deposited on top of the interlayer, intended to promote good electrical contact.

Inhibition of $Mo(S, Se)_2$ growth requires blocking of S(e) diffusion to the Mo layer. Thus, the interlayer must have a low bulk diffusion coefficient for S(e), including grain boundary contributions. Metal layers (unless monocrystalline or excessively thick) tend to be poor diffusion barriers due to fast grain boundary transport [61]. Inert compounds such as transition metal nitrides, borides, carbides, and silicides offer greatly improved barrier performance and chemical stability [61]. However, for extremely thin layers of such materials (in the order of 10 s of nm), large performance variations can be observed depending on the deposition method, which is ascribed to effects of grain boundary orientation, degree of oxidation, ability of complete coverage, and other process variables [62]. Importantly, any mechanical defects such as cracks or pinholes in the interlayer will reduce diffusion barrier performance. Such imperfections can be hard to avoid in very thin layers deposited on moderately rough surfaces, especially if thermal or mechanical stresses occur in subsequent processing steps [61].

For CZTS(e), it seems relatively easy to suppress $Mo(S, Se)_2$ formation by use of standard Ti-nitride or -boride interlayers [55, 63, 64], presumably due to reduced S(e) diffusivity in these materials. In this respect, the interlayers appear to act as effective diffusion barriers. In terms of Na transport, however, the picture is more complex. In several cases, Na transport was unaffected or even enhanced in the presence of interlayers [26, 50, 65]. There are several possible explanations for this. One is that the $Mo(S, Se)_2$ layer limits Na transport under normal conditions, with the result that if $Mo(S, Se)_2$ is avoided, Na diffusion is promoted. This interpretation supposes that the bulk diffusivity of Na in the interlayer is still large, while that for S(e) is small, which if true would be a fortunate coincidence! (We note that diffusivities *can* be highly element specific, although values for the relevant materials could not be found in literature). An alternative explanation is based on the aforementioned likelihood of defects such as pinholes in thin interlayers. Such features have indeed been observed for sputtered TiN [63] and Al_2O_3 [26] interlayers used for CZTS(e) back contacts. Thus, it is also possible that while the interlayer prevents S(e) from diffusing to most of the back contact, Na is able to diffuse via pinholes/cracks in the interlayer and spread into the CZTS(e) layer from there. In this situation, Na transport would be non-uniform, which could have detrimental effects for the electrical properties of the CZTS(e) layer. Since the Na content in the CZTS(e) is usually characterized by large-area/integral methods such as secondary ion mass spectroscopy (SIMS) [65] or x-ray photoelectron spectroscopy (XPS) profiling [26], it is not possible to distinguish between uniform transport via the interlayer itself and a non-uniform transport via mechanical defects. As noted by Englund *et al* [49], it may be preferable to prepare interlayers using techniques that deliver

better conformal coverage than sputtering, such as atomic layer deposition (ALD) or plasma enhanced chemical vapor deposition. Some authors, however, have claimed a positive effect of densely distributed openings in the interlayer, realizing a point contact scenario [26]. In any case, further attention should be paid to this matter to ensure that blocking of the $Mo(S, Se)_2$ formation does not come at the expense of a uniform Na incorporation.

2.3. Electrical properties of the back contact

In most kesterite devices, Mo is used as a back contact and as discussed above, due to the interaction with the chalcogens during the absorber formation process at elevated temperature, a relatively thick $Mo(S, Se)_2$ layer (>100 nm) is formed at the Mo/kesterite interface [6, 18–21, 25]. The impact of this layer on the photovoltaic properties (mainly reduction of the fill factor (FF) due to an increased series resistance (R_S) and an increase of the open circuit voltage (V_{OC}) deficit, and more generally the role of the back contact, is still under debate [66]. Although it is expected that the CZTSSe solar cell performance is reduced with increasing $Mo(S, Se)_2$ thickness [46, 51], state-of-the-art devices exhibit a relatively thick $Mo(S, Se)_2$ layer (see table 1). Record devices reaching a PCE of 12.6% contain a $Mo(S, Se)_2$ layer of ≈100 nm thickness [6]. Similarly, solar cells reaching a PCE of 11.2%, 11.8%, 11.6%, 11.4%, and 11.0% have $Mo(S, Se)_2$ layers of ≈200 nm [18], ≈250 nm [19], ≈200 nm [20], ≈990 nm [21], and ≈200 nm [25], respectively.

The Mo/$Mo(S, Se)_2$/CZTSSe contact has been suggested to be either ohmic [67, 68], to present a potential barrier [69, 70], or to form a reverse (n–p) diode [71]. The large variability in these models can be explained by the complexity of the $Mo(S, Se)_2$ material and of its interfaces with Mo and CZTSSe along with the lack of direct experimental measurements of the energy level alignment for this structure.

The anisotropy and layered structure of $Mo(S, Se)_2$ was mentioned in section 2.2 and figure 2. The orientation of the *c*-axis with respect to the layer plane has a very strong impact on the back contact properties. In undoped $MoSe_2$, the conductivity perpendicular to the *c*-axis (i.e. within the $MoSe_2$ layers) is 1500 times larger than parallel to the *c*-axis [72] (i.e. crossing from layer to layer). This anisotropy is, however, lowered in doped $MoSe_2$ [72, 73] which may be the most relevant case due to the inherent cationic diffusion during CZTSSe synthesis as discussed above. The 1.09 eV (1.23 eV) indirect bandgap energy of $MoSe_2$ (MoS_2) [74] can also be slightly varied depending on the orientation [72]. From theory, the Mo/$MoSe_2$ band alignment has been studied depending on the *c*-axis orientation [75]. A (0.2 ± 0.1) eV hole barrier is found when the *c*-axis is perpendicular to the substrate, while the Mo Fermi level is aligned with the valence band maximum (E_V) of $MoSe_2$ when the *c*-axis is parallel. Interestingly, this barrier is lowered in the presence of Na [75]. The effect of $MoSe_2$ orientation on the Mo/$MoSe_2$/absorber junction has been experimentally studied in the case of CIGSe technology [76, 77]. It was found that while the back contact/ absorber contact resistance is twice as low for the $MoSe_2$ *c*-axis parallel orientation, the influence of Na plays a more important role on the contact resistance than the $MoSe_2$ orientation. The impact of the $Mo(S, Se)_2$ orientation on the $Mo(S, Se_2)$/CZTSSe energy level alignment has not been studied, either theoretically or experimentally.

The $Mo(S, Se)_2$ conductivity is also under debate. The presence of an n-type or slightly p-doped semiconductor at the back contact may explain the reverse diode sometimes observed in the device characteristics [71, 78]. $Mo(S, Se)_2$ can indeed exhibit both p-type [79, 80] and n-type [72, 73, 81, 82] conductivity. The latter case was generally attributed to chalcogen deficiencies [79] even if the n-type behavior of MoS_2 due to S vacancies has been recently revised [83]. The different doping results found for $Mo(S, Se)_2$ films are probably due to impurities incorporated in the layer. Intercalation of atoms or molecules in the interlayer space of $Mo(S, Se)_2$ is one possibility for getting n-type conductivity [84], while substitution of Mo or S(e) inside the layer structure can give both n-type and p-type doping [85]. Experimentally it has been found that Re [86] and Cs [87] give n-type doping while oxygen [88], zinc [89], phosphorous [90], and niobium [91] give p-type doping. This extrinsic doping could be exploited to deliberately optimize the electronic structure of $Mo(S, Se)_2$ to improve the back contact properties.

Schematic band diagrams of the Mo/MoS_2/CZTS and Mo/$MoSe_2$/CZTSe back junctions proposed based on literature data are depicted in figures 3(a) and (b). Since energy level alignments derived from employing the simple electron affinity rule are in general not reliable [92], both band diagrams have been constructed using the best available estimates for the potential barrier at the Mo/$Mo(S, Se)_2$ interface and for the valence band offsets (VBO) at the $Mo(S, Se)_2$/kesterite interface. Lacking any direct measurements of the energy level alignment at the back contact/kesterite interface, the estimates are derived using the fact that, according to *ab initio* calculations, $E_V(CZTSe) - E_V(CIGSe) = 0.08$ eV [93], where E_v is the energy of the valence band maximum. In the absence of the corresponding calculated value for the sulfide counterpart, we use the same 0.08 eV offset in that case. Direct UPS measurements of the VBO at the $Mo(S_{0.6}Se_{0.4})_2$/$CIG(S_{0.9}Se_{0.1})_2$ and $MoSe_2$/CIGSe interfaces reveal that $E_v(CIGSe) - E_v(MoSe_2) = -0.03$ eV and $E_v(CIG(S_{0.6}Se_{0.4})_2) - E_v(Mo(S_{0.9}Se_{0.1})_2) =$ 0.12 eV, respectively [82]. Combining these numbers, the estimates for the desired VBO are: $E_v(CZTSe) - E_v(MoSe_2) = 0.05$ eV and $E_v(CZTS) - E_v(MoS_2) = 0.20$ eV. Note that this approach does not consider effects

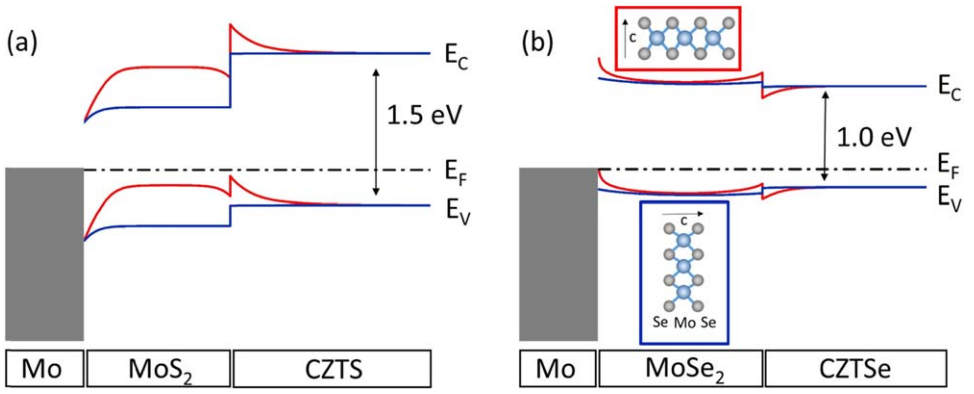

Figure 3. Band diagram (conduction band minimum E_C, valence band maximum E_V and Fermi level E_F) of kesterite back contacts: (a) $Mo/MoS_2/CZTS$ junction for two different Fermi level positions in the MoS_2 (E_F–E_V = 0.55 eV, blue curves; E_F–E_V = 0.15 eV, red curves) (b) $Mo/MoSe_2/CZTSe$ back contact with a slightly p-type (10^{13} cm^{-3}) doped $MoSe_2$ and different $MoSe_2$ crystal orientations [74].

caused by interface formation. Furthermore, it is assumed that the VBO for the $MoSe_2$/CIGSe interface [82] is measured with a parallel $MoSe_2$ orientation; VBO for the perpendicular orientation has been shifted corresponding to [75]. In real devices, intermediate orientations and randomly distributed orientations for different $Mo(S, Se)_2$ grains is also possible.

For the Mo/MoS_2 interface a rather large hole barrier of 0.84 eV is used in figure 3(a) according to the results of a XPS/UPS study [81]. The last parameter needed to construct the band diagram is the Fermi level position (E_F) in $Mo(S, Se)_2$. To show the relevance of this parameter, we report in figure 3(a) the band diagrams for two different scenarios: low p-doped MoS_2 ($E_F - E_V = 0.55$ eV, blue curves) and high p-doped MoS_2 ($E_F - E_V = 0.15$ eV, red curves). The figure clearly shows that a high p-type doping of MoS_2 leads to a band bending that is able to reflect the photogenerated minority carriers (i.e. electrons) from the MoS_2/CZTS interface and to induce a hole accumulation layer, which would allow a good Ohmic contact if the Mo/MoS_2 barrier is sufficiently narrow to allow for efficient charger carrier tunneling. In contrast, a poorly doped MoS_2 can increase the minority carrier recombination velocity and introduce a barrier for the hole transport across the heterojunction, which could be the reason for anomalous current–voltage (J–V) curves (i.e. roll-over or S-shaped curve) [78].

For the $Mo/MoSe_2$ interface, the theoretical values from [75] have been used for both extreme $MoSe_2$ orientations to derive the respective energy level alignment. $MoSe_2$ is assumed to be slightly p-doped without Fermi level pinning. Within this configuration, a small (0.2 eV) barrier for holes exists at the $Mo/MoSe_2$ interface for perpendicular c-axis orientation, while no barrier is present in the parallel orientation case. This result is quite different from the one just reported for the sulfide case and from simulations based on electron affinity values [68], emphasizing that direct measurements of the energy level alignment at the kesterite back interface are crucially needed to better understand limitations arising from the back contact.

Some experiments have been made trying to replace the back contact metal (Au, W, Pt, Pd, Ni) [15]. However, these efforts did not lead to device improvement as seen in table 1. Finally, recent works [13, 80] show that for reduced absorber thicknesses, replacing the $Mo/Mo(S, Se)_2$ back contact with a high work function material (MoO_3) can significantly improve the device performance (table 1), but necessitates an exfoliation step of the absorber.

2.4. Transparent back contacts

As discussed above, Mo is still the most common back contact material for kesterites. For applications where a transparent back contact is required, such as bifacial or multijunction solar cells, Mo has to be replaced by another material that combines good electrical conductivity with optical transparency and withstands kesterite processing conditions. Despite the intense research effort on alternative materials, conventional TCOs remain the most common transparent conductors [94].

Present TCOs are based on three binary oxides, SnO_2, In_2O_3, or ZnO [95]. Because undoped binary oxides suffer from limited temperature stability and difficulties with accurate compositional control, impurity doped variants are commonly employed. Indium tin oxide (ITO) is the most effective TCO that combines excellent electrical properties with good chemical stability. The price of indium and concerns over its availability, however, spurred a search for In-free alternatives. Aluminum doped zinc oxide (ZnO:Al) is a common replacement with conductivity reaching that of ITO. The chemical stability of ZnO:Al is, however, generally

lower than that of In_2O_3 [96]. ZnO is also more reactive towards oxygen than In_2O_3 and therefore requires a more strict control of the oxygen supply during deposition [97]. F doped SnO_2 (FTO) offers exceptional chemical stability, high hardness, and excellent thermal stability although the minimum resistivity of $5 \times 10^{-4}\,\Omega$ cm is higher than the best values achieved for ZnO:Al and ITO ($10^{-4}\,\Omega$ cm) [98].

Kesterite solar cells using FTO and ITO as transparent back contacts have been reported. Sarswat [99, 100] studied CZTS on FTO back contacts and showed that in the presence of S the FTO degraded at temperatures above 500 °C. The conductivity decrease, however, was less pronounced for FTO coated with CZTS precursors compared to bare FTO. Furthermore, the S pressure had a strong influence as demonstrated in an experiment where FTO samples were placed at different distances from a S source during annealing. The highest resistivity increase was observed for FTO closest to the S source with a clear relation between the distance and resistivity increase. The FTO was stable when annealed in vacuum or Ar up to 600 °C, [100] indicating the presence of free S as the main cause of FTO degradation.

In a study comparing FTO and ITO, Kim *et al* [24] demonstrated CZTSe bifacial solar cells and reported better stability of the FTO contact than of the ITO contact at selenization temperatures up to 500 °C. However, both FTO and ITO provided a non-Ohmic contact that led to a V_{OC} loss. There was a pronounced difference in the interfaces between CZTSe and the two back contacts. FTO resulted in a voided interface and low adhesion of the absorber. ITO, in contrast, provided a smooth interface with good adhesion. Mechanically strong interfaces are, however, often a sign of a chemical interaction between the adjacent layers. Ge *et al* [101] analyzed interfacial reactions between CZTSe and ITO, and indeed, confirmed indium incorporation in CZTSe and the formation of a SnO_2 layer at the interface. The use of ITO is therefore limited by indium diffusion into CZTSe. Interestingly, bare ITO was stable in Se atmosphere up to at least 550 °C.

Limited temperature stability of the TCO in chalcogen atmospheres requires reduction of the annealing temperature. This, however, has a negative impact on the absorber quality. Therefore, the use of a more stable barrier layer to prevent the interface reactions has been investigated [50]. A thin, high work-function MoO_x interface layer can improve contacts in solar cells [102]. Espindola-Rodriguez *et al* [8] utilized thin Mo interlayers on FTO for CZTSSe. While the sheet resistance of a bare FTO increased from 10 to 700 $\Omega\,sq^{-1}$. upon annealing in S + Se + Sn at 550 °C, the resistance of FTO films with a 20 nm thick Mo interlayer decreased. The interlayer led to an efficiency improvement from 3.1% to 7.6% for a bifacial solar cell. The use of Mo, however, reduces the back contact overall transparency and the performance of thinner layers needs to be investigated.

In summary, surprisingly little research has been published on transparent back contacts for kesterite solar cells and even for the more mature chalcopyrite absorbers this area is not very much explored [96, 103]. In addition to the use of different passivation layers, the question of Na supply needs to be addressed. TCO layers have often much lower permeability for Na than the standard Mo back contact [104] and differences in the Na concentration further complicate comparison of the device performance.

3. Front contact

An overview of device results for some of the different front contacts that have been studied for kesterite solar cells is given in table 2. The table includes highest reported device efficiencies for CZTSSe, CZTSe, and CZTS with their reported buffer layer and TCO stacks as well as alternative buffer layers with their corresponding CdS buffer reference devices, if reported. In the sections below, the results on (alternative) buffer materials, the energy level alignment at the CZTSSe/CdS interface, and interface treatments are discussed.

3.1. TCO contacts

TCO layers on top of buffer/CZTSSe heterostructures (as shown in figure 1) are needed to enable efficient collection of photogenerated electrons. Generally, these consist of resistive/undoped ZnO (≈50–80 nm) covered with either ZnO:Al or ITO. As seen in table 2, for the best small cells with metallic grids, the highly conductive TCO (i.e. ZnO:Al or ITO) layer thickness is between 50 and 200 nm, thereby fulfilling transparency and conductivity requirements. These two TCOs, although showing rather similar band gaps (≈3.5 eV), differ in their transparency within the range of the exploited solar spectrum (300–1300 nm) and their work function values. This latter parameter is critical for the device operation since it is related to the electronic structure in the CZTSSe/emitter interface region. According to Klein *et al* [119], the Fermi level relative to the vacuum level of ZnO:Al films ranges from ≈2.4 eV to as high as ≈3.8 eV, and those of ITO films range from ≈2.0 to ≈3.5 eV. These values are strongly dependent on crystal orientation, thus on deposition technique and growth conditions, as well as on post deposition treatments (e.g. annealing). While direct comparisons of ZnO:Al and ITO contacts for otherwise identical device stacks show only minor differences in performance [78], the higher thermal stability of ITO could be advantageous in certain circumstances (see section 2.4).

Table 2. Device results (total area PCE, open circuit voltage [V_{OC}], short circuit current density [J_{SC}], and fill factor [FF]) for different buffer layer materials, produced by chemical bath deposition (CBD), successive ionic layer adsorption and reaction (SILAR), spray pyrolysis or atomic layer deposition (ALD) methods. The table includes record and high efficiency devices with standard CdS buffer layer and alternative buffer layers compared to CdS ('CdS ref'), if data is available. Data is given for CZTSSe, CZTSe, and CZTS-based devices with or without anti reflective coating (ARC). The stated band gap energies (E_g) are derived from quantum efficiency measurements reported in the respective references. In cases in which not all information was given in the cited sources, the cells in the table are intentionally left blank.

Window layer	Buffer deposition method	Buffer material	CZTSSe E_g (eV)	V_{OC} (mV)	FF (%)	J_{SC} (mA cm^{-2})	PCE (%)	ARC	Area (cm^2)	References
				CZTSSe						
i-ZnO/ITO 10/50 nm	CBD	CdS 25 nm	1.13	513	69.8	35.2	12.6	Yes	0.42	[6]
	CBD	CdS		533	63.0	33.6	11.3		1.176	[7]
	CBD	CdS		541	65.9	35.4	12.6		0.48	[7]
i-ZnO/ZnO:Al	CBD	ZnS(O,OH)	1.12	389	52	29	5.2 LS	No	0.5	[105]
i-ZnO/ZnO:Al	CBD	CdS ref	1.12	376	55	34	7	No	0.5	[105]
i-ZnO/ITO	CBD	In_2S_3/CdS	1.07	471	70.3	37.1	12.3	Yes		[106]
i-ZnO/ITO	CBD	In_2S_3		424	55	32.3	7.59	Yes		[107]
i-ZnO/ITO	CBD	CdS ref		465	62	27.1	7.75	No		[107]
i-ZnO/ZnO:Al	ALD	$ZnSnO_x$		414	60.8	34.1	8.6			[108]
i-ZnO/ZnO:Al	CBD	CdS ref		404	60.4	32.6	8.1			[108]
i-ZnO/ITO	CBD	ZnMgO	≈1.17	440	42	29.3	5.4	No	0.25	[109]
i-ZnO/ITO	CBD	CdS ref	≈1.17	480	65	29.3	9.1	No	0.25	[109]
				CZTSe						
i-ZnO (ALD) /ZnO:Al 50/350 nm	CBD	CdS (30 nm)	1.0	423	66.6	41.7	11.7	Yes	0.522	[110]
i-ZnO/ZnO:Al 50/400 nm	CBD	CdS (50 nm)	1.07	432	76.2	36.3	11.95	No	0.52	[17]
	CBD	Zn(O, S)	1.02	358	60.0	33.5	7.2	Yes	0.345	[111]
	CBD	CdS ref	1.02	388	57.9	35.9	8.0	No	0.345	[111]
i-ZnO/ZnO:Al 80/600 nm	CBD	ZnS(O, OH)		379	55.9	30.7	6.5 LS	No	0.09	[112]
i-ZnO/ZnO:Al 80/600 nm	CBD	CdS ref		401	56.3	30.5	6.9	No	0.09	[112]
i-ZnO/ITO	Spray pyrolysis	In_2S_3	1.08	430	47.7	28.3	5.7	No	0.1	[113]
				CZTS						
i-ZnO/ITO 60/240 nm	CBD	CdS		708	65.1	21.8	10.0	Yes	1.113	[25]
i-ZnO/ ITO 60/240 nm	CBD	CdS		731	69.3	21.7	11.0	Yes	0.23	[25]
ZnO:B	CBD	Zn-based		593[a]	50.2	19.6	5.8[b]	No	15.2	[114]
ZnO:B	CBD	In-based		653[a]	53.0	18.3	6.3[b]	No	15.2	[114]
i-ZnO/ITO 60/200 nm	SILAR	CdZnS	1.5	748	63.2	19.5	9.2[b]		0.3–0.4	[115]
i-ZnO/ITO 60/200 nm	CBD	CdS ref	1.5	665	57.4	20.4	7.8		0.3–0.4	[115]
i-ZnO/ITO	CBD	In_2S_3	1.4	621	54.5	20	6.9	No		[116]
IZO/ITO 60/200 nm		In_2S_3/CdS		714	52.7	17.6	6.6		0.3–0.4	[117]
IZO/ITO 60/200 nm		CdS ref		641	53.7	15.9	5.5		0.3–0.4	[117]
i-ZnO/ZnO:Al 80/200 nm	ALD	$Zn_{1-x}Sn_xO_y$	1.55	746	68.0	19.1	9.7	Yes	0.09	[118]
i-ZnO/ZnO:Al 80/200 nm	CBD	CdS ref	1.55	715	64	16.4	7.5	No	0.09	[118]
i-ZnO/ZnO:Al 80/200 nm	ALD	$Zn_{1-x}Sn_xO_y$	1.64	778	56.4	16.3	7.1	No	0.09	[118]
i-ZnO/ZnO:Al 80/200 nm	CBD	CdS ref	1.64	809	61.2	17.0	8.4	Yes	0.09	[118]
i-ZnO/ITO 50/210 nm	ALD	$Zn_{1-x}Sn_xO_y$	1.5	720	63.5	20.4	9.34	Yes	0.224	[53]
i-ZnO/ITO 50/210 nm	CBD	CdS ref	1.5	652	64.2	16.5	9.90	No		[53]

[a] Derived from the module performance;

[b] Active area PCE.

3.2. CdS buffer layers by chemical bath deposition (CBD)

A CdS layer prepared by CBD is still the standard buffer used in the record devices for all compositions of CZTSSe as seen in table 2. In the 12.6% device [6] and 11.6% CZTSe device [20] the CdS thickness was optimized to 25 nm, which is thinner than commonly used. For the CZTS record of 11% [25], a 50–60 nm thick CdS was used followed by an annealing step in N_2. In all three cases, a ZnO/ITO contact stack was used on top of the CdS.

3.2.1. Energy level alignment at the kesterite/CdS interface

Since the photogenerated electrons have to pass the CZTSSe/CdS interface, the energy level alignment, especially of the conduction bands (CB), is crucial. Just as the optical band gap, i.e. the separation between valence band maximum (E_V) and CB minimum (E_C), can easily be tuned by the [S]/([S]+[Se]) ratio of the absorber, also the offsets between the E_V and E_C energy levels of the kesterite and the CdS buffer layer can be expected to change. Figure 4 shows reported VB and CB offsets (VBO: circles and CBO: triangles) between CdS and CZTSSe as a function of the [S]/([S]+[Se]) ratio of the absorber [93, 120–127]. The black symbols indicate results from direct measurements of the VBO by means of UV (UPS) or x-ray (XPS) photoelectron spectroscopy and CBO by means of inverse photoemission spectroscopy from [120–124] (see [128] for more details on the methodology). The red symbols represent alignment data based on the direct determination of the VBO (by UPS or XPS) and an *estimated* CBO derived by adding the difference of the optical band gaps (ΔE_g) of CdS and CZTSSe to the VBO [125–127]. Note that the accuracy of this estimation strongly depends on the assumption that the optical bulk band gaps of the involved junction partners is the same as the electronic band gaps at the surface/interface. At least for CZTS kesterites [120, 129], it has been shown that this assumption is legitimate (which is in contrast to that which has been reported for high-efficiency chalcopyrite absorbers [130]). Finally, the blue symbols indicate the energy level alignment according to density functional theory calculations [93]. Note that there is quite some energy level alignment data reported for the interface between CdS and S-free CZTSe as well as Se-free CZTS absorbers, but only one data point for the kesterite/CdS junction with an intermediate [S]/([S]+[Se]) absorber ratio of 0.28 [122]. Without going into detail of why the determined CBO and VBO values vary somewhat in the cases where more than one data point is available (most of it can certainly be ascribed to the variations in absorber composition across laboratories and employed preparation routes), we find it possible to describe the [S]/([S]+[Se]) driven CBO and VBO evolution with confidence envelopes (depicted as gray hatched areas in figure 4) that have an uncertainty of approximately $\pm$0.25 eV. Considering that the experimental uncertainty of directly determining VBO and CBO for one specific CZTSSe/CdS interface is in the order of $\pm$0.15 eV, it is remarkable that the derived envelopes are able to cover all alignment data—even the calculated ones. The only exemptions are the measurements by Haight *et al* [131] that are based on femtosecond laser pump-probe UPS measurements (fs-UPS, dotted line in figure 4) of the VBO and estimated CBO $=$ VBO $+$ ΔE_g values. While the energy level alignment derived for the S-free CZTSe/CdS heterojunction agrees with the other data and lies within the confidence envelope, the VBO and CBO values derived for other CZTSSe/CdS interfaces (with [S]/([S]+[Se]) $> \approx 0.3$) significantly deviate. Especially the general observation of negative CBO values at the CZTS/CdS interface clearly contradicts the results of Haight *et al* reporting a pronounced positive CBO [131]. A detailed comparison of the data from [120, 131] reveals that while a similar CZTS E_V was found ($\approx$ –0.6 eV), the fs-UPS derived (unpumped) E_V position of the CdS on the Cu_2ZnSnS_4 (–1.14 eV [131]) significantly differs from that derived by standard UPS (–1.65 [$\pm$0.10] eV [120]). Thus, either the CdS material properties were completely different (p-type instead of n-type) or the thin (5 nm) CdS layer was not sufficiently thick for the fs-UPS measurements to prevent the VB edge of the underlying CZTS absorber to impact the E_V determination. Another explanation could be that the pump-probe approach might result in an overestimation of CBO if the surface/interface is particularly defect-rich causing a Fermi level pinning [132]. Indeed, while the interface-induced band bending (iibb, see [128]) is found to be $> +0.4$ eV [122, 124] for the CZTSe/CdS heterojunction, iibb seems to be limited to (0.0 ± 0.1) eV [120] for the CZTS/CdS interface. This indicates that, while the Fermi level can to some extent move freely upon the deposition of CdS at the interface to the S-free kesterite absorber, it seems to be pinned at the CZTS/CdS interface. This explains the observed VBO and CBO agreement for the CZTSe/CdS and the disagreement for the CZTS/CdS case.

The large negative VBO found for all CZTSSe/CdS interfaces independent of the absorber [S]/([S]+[Se]) composition is beneficial for the solar cell performance as it acts as hole mirror preventing holes migrating into the emitter (where they would recombine). In contrast, the CBO changes from being positive for low S contents (i.e. the E_C of CdS is above that of the absorber, also known as a 'spike-like' CBO) to be negative for high [S]/([S]+[Se]) ratios (i.e. the E_C of CdS is below that of the absorber, also known as a 'cliff-like' CBO). According to device simulation for chalcopyrite TFSCs [133–135], the CBO range that is compatible with high-efficiency devices is (-0.1 to $+0.3$) eV, indicated as green hatched area in figure 4. If the CBO is lower than -0.1 eV, the probability to form a high-rate charge carrier recombination path across the cliff-like interface increases. Similarly, a large spike-like CBO of $>+0.3$ eV will increasingly limit device performance due to becoming an

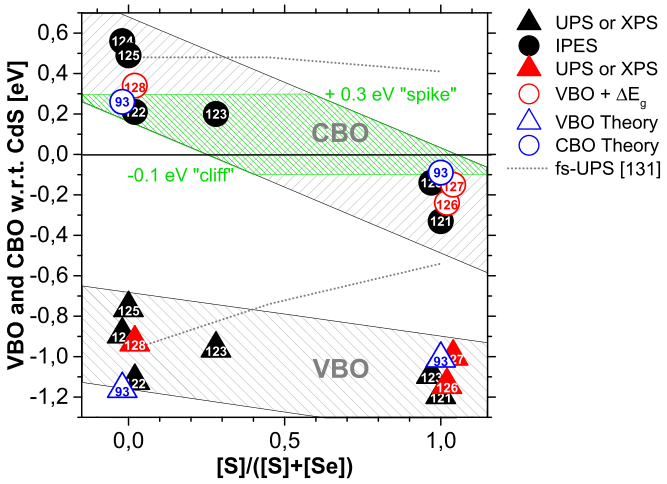

Figure 4. Valence band (VBO, circles) and conduction band (CBO, triangles) offsets between CdS and CZTSSe as a function of the [S]/([S]+[Se]) ratio of the absorber reported in [93, 120–127]. The black symbols indicate results from direct measurements of the VBO—by means of UV (UPS) or x-ray (XPS) photoelectron spectroscopy and CBO—by means of inverse photoemission spectroscopy (IPES). The red symbols represent alignment data based on the direct determination of the VBO (by UPS or XPS) and an estimated CBO derived by adding the difference of the optical band gaps (ΔE_g) of CdS and CZTSSe to the VBO. The blue symbols represent VBO and CBO values derived by density functional theory calculations. The dashed lines indicate the results based on femtosecond laser pump-probe UPS (fs-UPS) measurements of the VBO and correspondingly estimated CBO values [128]. The gray hatched area represents confidence envelopes for the [S]/([S]+[Se])-driven VBO and CBO evolution and the green hatched area represents the CBO range that is compatible with high-efficiency solar cells.

energetic barrier for electron transport. As can be seen in figure 4, most of the CBO data points are outside of the acceptable CBO range, especially for the CZTS/CdS heterojunction. However, it seems that for CZTSSe absorbers with low/intermediate [S]/([S]+[Se]) (or even S-free) absorber compositions, the CBO criteria can be fulfilled. As a matter of fact, the highest efficiencies for CZTSSe/CdS based thin-film solar cells have been achieved with [S]/([S]+[Se]) absorber compositions of ≈0.3 [6] for which the data from [123] in figure 4 could be representative. In conclusion from the absorber/buffer energy alignment point of view, there is no reason why kesterite-based thin-film solar cells using absorbers with [S]/([S]+[Se]) composition ≈0.3 might not reach similar high efficiencies as chalcopyrite-based devices. Hence, the apparent open circuit voltage deficit of state-of-the-art kesterite solar cell devices has to be explained differently, e.g. by other less ideal interfaces in the devices (addressed in section 2.3), interface defects or by (deep) defects (as done in other contributions to this special issue).

3.2.2. Chemical interface treatments of the heterojunction

Even if the champion kesterite solar cells reported until now use CdS as standard buffer layer, there are several studies showing large effects on device performance upon different interface treatments such as absorber etching or annealing of the absorber/buffer heterojunction or the whole device stack. Selective etching of secondary phases from the kesterite surface is commonly used. For example, potassium cyanide (KCN) is used to remove $Cu_{2-x}S$-phases; $KMnO_4$, H_2SO_4 and Na_2S have been used to remove ZnSe [136]; and aqueous ammonia can be employed to remove surface oxides [137]. Most of these treatments can also remove Na-compounds from the kesterite surface. For CZTS, a correlation between effective removal of Na_2S by KCN etching or oxidation followed by rinsing, and more uniform CdS growth was shown [138]. Etching could also influence the CZTS surface properties, and an increased surface band gap was for example reported for Cu-poor CZTS after KCN etching [139].

3.2.3. Annealing of the heterojunction

Annealing at temperatures around 100 °C–400 °C before or after buffer layer deposition has shown strong impact on device performances as seen in table 3. While certain effects from such annealing could be linked to the order–disorder transition in bulk CZTSSe with critical temperature at around 260 °C or 200 °C for the pure sulfide (CZTS) or selenide (CZTSe) compound, respectively [140, 141], this needs to be monitored and decoupled from other annealing induced effects for better understanding. For example, V_{OC} and J_{SC} variations can be related to order–disorder induced variations in the band gap energy of the absorber, which can reach 200 meV in CZTS [142] and 110 meV in CZTSe [141]. However, since this is a bulk effect, covered in other contributions of this special issue, it will not be discussed in depth here.

Table 3. Influence of different post-deposition annealing treatments on device parameters. V_{OC}, FF, J_{SC}, and PCE values are reported for as deposited (in parentheses) and annealed devices. The results shown in the last row of the table indicate the performance after an ordering anneal compared to that after a disordering anneal (in parenthesis) at 300 °C on a hot plate for 15 min.

Stack annealed	Annealing para-meters	V_{oc} (mV)	FF (%)	J_{sc} (mA cm^{-2})	PCE (%)	References
CZTSe/CdS	200 °C, air, 20 min	408 (316)	45 (30.6)	28 (22.1)	6.1 (1.8)	[136]
CZTSe/CdS/ZnO/ITO	200 °C, air, 35 min	405 (331)	63.2 (29.0)	28.3 (19.0)	7.3 (1.8)	[136]
CZTS/CdS	Laser dose: 24.5 J cm^{-2}	536 (572)	60 (54)	17.4 (14.8)	5.6 (4.6)	[143]
CZTS	Laser dose: 34.30 J cm^{-2}	664 (674)	56.0 (55.5)	19.7 (18)	7.3 (6.7)	[143]
CZTS/CdS	230 °C	700 (720)	63 (43)	21.3 (16.0)	9.4 (5.0)	[144]
CZTS/CdS	270 °C, N_2, 10 min	730 (670)	65 (54)	21.7 (20.7)	11.0 (7.8)	[25]
CZTSSe	200 °C, N_2, 30 min	414 (378)	62.7 (47.6)	34.0 (30.6)	8.8 (5.5)	[145]
CZTS/CdS/ZnO/ITO	160 °C, N_2, 24 h	702 (642)	43.1 (64.0)	16.3 (19.3)	4.9 (7.9)	[78]

Annealing of the absorber layer in air prior to buffer layer deposition has been shown to improve device performance by several groups [137, 145–148]. Sardashti *et al* [137] performed annealing in air at 300 °C–400 °C, followed by etching in NH_4OH to achieve high performance devices (note that the performance of reference cells without air anneal was not given). The benefit of the air anneal was ascribed to the passivation of GB by SnO_x and a reduced Cu content. In a comparison of air annealing treatments of bare CZTS and CZTSe absorbers, Zn-enrichment was seen after NH_4OH etching in both cases, while removal of elemental selenium was only observed for CZTSe [146]. Higher annealing temperatures were beneficial for the selenide absorber and the efficiency improvements were also larger for CZTSe cells.

Annealing in N_2 at different temperatures has also been used to improve device performance. An optimum temperature of 200 °C was found for the annealing of CZTSSe. The improved device performance was ascribed to an increased photoluminescence intensity and an increased carrier concentration, i.e. probably related to improved bulk properties [145]. In other studies using N_2 annealing of bare absorbers, degradation of device performance was seen for low temperature and improvement seen above 200 °C [148] or 125 °C [147]. Changes in Na distribution and carrier concentration were reported, again suggesting that at least part of the improvement is related to bulk properties.

Annealing after buffer layer deposition, or of the full device stack, has also shown improvements. Tajima *et al* have studied annealing and the compositional distributions at CZTS cell interfaces by using atom-probe tomography [149] suggesting annealing-induced Cd diffusion into the CZTS layer. A segregation of Zn at the CZTS/CdS interface, and a change of oxygen and hydrogen concentrations in the CdS layer depending on the annealing temperature were also observed. Another study reported that annealing after the CdS deposition at 573 K improved the photovoltaic properties of CZTS cells (table 3), presumed to be due to the formation of a heterophase epitaxial junction between a solid-solution of $Cd_{1-x}Zn_xS$ and CZTS and the elimination of Cd(S, O, OH) [149]. The same group has investigated the effects of the CdS buffer layer thickness and annealing conditions on photovoltaic properties of CZTS cells. They showed that for 40 nm thick CdS layers that were post-annealed at 603 K, the J_{SC} of respective cells improved significantly. The best-performing cell exhibited a PCE of 9.4% as seen in table 3 [144]. The authors discussed that Cd diffusion from CdS into CZTS and Zn diffusion from CZTS into CdS during the annealing could improve the energy level alignment at the CZTS/CdS interface (see section 3.2). The main improvement was in J_{SC} and FF, while V_{OC} was slightly reduced as compared to the non-annealed case. Annealing of the full CZTS device stack at 160 °C in N_2 to induce ordering of the CZTS resulted in severe FF loss and S-shaped *J–V* characteristics in addition to the expected reduction in J_{SC} and increase in V_{OC} due to increased band gap energy of the absorber [78]. The effect was reversible upon disordering of the devices and was tentatively ascribed to a blocking back contact barrier due to poor p-type doping of MoS_2 (see section 2.3).

Huang *et al* [143] have reported a novel diode laser annealing method as a post-sulfurization heat treatment on pure-sulfide CZTS, fabricated by sputtering deposition, with a CdS capping layer. After receiving an ultra-fast laser scan treatment, the crystallinity of the CZTS film was improved and the PCE of the laser-annealed device was increased from 4.6% to 5.6%. A J_{SC} increase from 14.8 to 17.4 mA cm^{-2} after laser treatment was the main reason for this improvement [143]. The increase was connected to improved long wavelength collection as seen from quantum efficiency, i.e. probably related to improvements of the CZTS bulk properties. Laser annealing prior to CdS buffer deposition could also improve device performance, again mainly due to increased current and long wavelength collection. Lower laser doses had to be applied to samples with CdS capping layers since degradation of the CdS was observed for high doses (table 3).

Yan *et al* [25] have employed a post deposition heat treatment of the CZTS/CdS heterojunction aiming to reduce the heterojunction non-radiative recombination. They obtained sulfide CZTS solar cells with record efficiency of 11% for small area cells (0.23 cm^2) and 10% for a standard sized cell (1.11 cm^2) [25], see table 2. This

approach enables elemental inter-diffusion, leading to a Zn gradient within CdS and a Cd gradient within CZTS, as well as a Na accumulation and local Cu-depletion at the heterojunction. The approach also leads to the formation of new phases: Cd diffusion into the lattice of CZTS surface forms a thin layer of $Cu_2Cd_xZn_{1-x}SnS_4$ while Zn diffusion into the CdS is suggested to form ultrathin $Zn_xCd_{1-x}S$. The authors also report the possible formation of a new phase of $Cu_{2-x}Na_xZnSnS_4$ (average $x \approx 0.07$) nanoclusters.

In the case of CZTSe, Neuchitzer *et al* [136] studied the strong influence of surface etching combined with post deposition low-temperature annealing of CZTSe absorbers, CdS buffer layers, and the CZTSe/CdS interface. A change in surface composition was seen together with an improvement in device efficiency from below 3% to up to 8.3% (table 3). In addition to changes in the Cu surface concentration, transmission electron microscope electron energy loss spectroscopy mapping showed a reduction of Cu in the GB after the annealing treatment. This annealing induced change towards a more benign composition of the GB could possibly explain the gain in V_{OC} compared to non-annealed devices.

In summary, annealing of the kesterite absorber or heterojunction can significantly improve device performance, but the underlying reasons are in general not clear, and may be very specific for certain preparation routes. Effects like redistribution of alkalis (such as Na), oxidation, Cu-removal from GB, removal of secondary phases by combined annealing and etching, and intermixing at the heterojunction have all been discussed and could all have a significant impact on the electronic structure of the device stack and thus the device performance. Further dedicated studies to separate these effects and establish clear structure function relationships are crucially required.

3.2.4. Absorber doping as part of the interface formation process

Doping of the kesterite absorber by extrinsic elements such as alkali metals and indium have been employed and in some cases led to improved device performance. While this is not directly part of the properties of the contacts, the doping elements have in some cases been introduced as part of the buffer layer deposition process. One example is the demonstration of improved performance by an ultrathin layer of In_2S_3 deposited on top of the standard CdS buffer layer, followed by brief annealing (seconds to minutes) at 250 °C–300 °C [106]. Significant diffusion of indium into the CdS buffer layer and the hydrazine-processed CZTSSe absorber was evident. This indium doping was claimed to be one reason for the observed increase of the carrier concentration in both, the buffer and absorber layer. This doping relieved the typically observed collapse of efficiency for temperatures below 200 K and V_{OC} saturation with increasing illumination intensity, caused by the low conductivity of pristine CZTSSe [106].

In case of doping by alkalis, it is worth noting that if the kesterite absorber is synthesized via a wet-chemical route, the doping process can be relatively easy, because the alkaline element can be dissolved into the precursor solution using the desired quantity. On the contrary, when the kesterite absorber is synthesized by physical means, the alkaline doping process requires additional steps (pre or post deposition treatments), and the accurate control of the alkaline concentration is rather difficult [17]. Comparison of the pre deposition application of NaF, followed by high temperature selenisation, with post deposition application of NaF, followed by annealing at 300 °C, showed a V_{OC} and carrier concentration increase in both cases as compared to Na-free reference cells [150]. This is similar to CIGSe devices, where the beneficial effect from Na on crystallization at high temperature was decoupled from the beneficial effect on optoelectronic properties by using post deposition application routes of Na [151]. Sánchez *et al* have proposed an innovative alkali doping strategy for CZTSe. Different concentrations of alkali dopants Li, Na, and K were introduced into the CdS buffer layer during the CBD process that then diffused into the kesterite during a low-temperature annealing process. A complete composition analysis was carried out by combining XPS and SIMS that showed a clear incorporation of the alkaline elements into the CdS thin films, and their diffusion into the kesterite absorber. The diffusion of the alkaline elements depends on their atomic weight (Li $<$ Na $<$ K) and has a strong impact on the CdS morphology (coverage and bump-like defects) as well as its optical (transmission and bandgap energy) and structural properties. In addition, a large impact on the electronic properties of the devices was observed, including a strong modification of the charge-carrier density (from capacitance-voltage-measurements) which increased with increasing the concentration of the doping agent, confirming the effectiveness of this doping method, and resulting in a significant PCE enhancement reaching values up to 10.1% [18].

3.3. Cd-free alternative buffer layers

As discussed above, chemical bath deposited (CBD) CdS buffer layers have resulted, so far, in the highest device performance for kesterite-based TFSCs. This is similar to the case for CIGSe TFSCs even if the latest record of 23.35% is Cd-free [152]. There are several issues associated with the CBD-CdS buffer layer in terms of environmental impact. Additionally, it has a narrow bandgap of ≈2.4–2.5 eV that results in parasitic absorption of the incident UV photons, limiting device performance. In the case of S-rich absorbers, it also limits the device

performance owing to the cliff-like CBO at the absorber/buffer interface as discussed above (section 3.2 and figure 4). Therefore, significant efforts have been devoted toward the investigation of Cd-free alternative buffer layers for kesterite-based TFSCs. In this regard, as seen in table 2, several research groups have already shown an enhanced device performance in the case of S-rich absorbers by replacing the CdS layer with larger band-gap $Zn_{1-x}Sn_xO_y$ buffer layers.

3.3.1. ZnS-based buffer layers

The application of a CBD-ZnS buffer layer was reported by Nguyen *et al* [153] for CZTSSe-based monograin TFSCs reaching PCEs of 4.5% for a single layer of 10–25 nm ZnS buffer, which was very close to the performance of the reference cell with single layer CdS buffer (≈4.8%). However, a similar study with CBD-ZnS for CZTSSe TFSCs showed lower PCE of 3.84% as compared to the CdS-reference device (5.25%) [154]. The lower performance was possibly due to the difference in microstructure and compositions of the absorbers and/or the buffers. However, a sputter-deposited ZnS buffer layer showed an even lower PCE of 2.11% for CZTS-based TFSC [155].

A few ternary materials have shown potential as alternative buffer candidate material for kesterite-based TFSCs. They have the advantage of having (optoelectronic) properties that can easily be tuned by controlling their stoichiometry [156–161]. For Zn(O, S) buffer layers prepared by ALD, e.g. the S/O ratio can easily be varied. However, kesterite devices with ALD Zn(O, S) buffer layers have not yet shown high PCEs [156, 159, 160]. Recently, Zhang *et al* [157] fabricated CZTS-based TFSCs with ozone assisted photochemical deposited Zn(O, S) buffer layers having a band gap ranging between 3.3–3.7 eV, tuned by a variable ozone flow rate. A significant improvement in V_{OC} was observed compared to that of reference devices with ZnS and CdS buffer layers, but the overall efficiency was low. Li *et al* [158] reported a large improvement in the performance of CZTSe-based TFSCs with CBD-Zn(O, S) buffer layers when they were treated with concentrated aqueous ammonia and subject to subsequent low-temperature annealing. A maximum PCE of 6.57% was achieved for the respective device (8.04% for the CdS reference device). These post-deposition treatments were performed to reduce ZnO and $Zn(OH)_2$ phases in the CBD-Zn(O, S) buffer layer. Successful demonstration of a Zn-based buffer layer by CBD was also reported by Hiroi *et al* for a CZTS submodule [114] and by Grenet *et al* for CZTSSe [105] as shown in table 2. Neuschitzer *et al* [162] demonstrated the application of CBD-ZnS(O, OH) for CZTSe TFSCs, which revealed a promising device performance due to higher J_{SC} as compared to that of a cell with the standard CdS buffer layer.

3.3.2. $Zn_{1-x}Sn_xO_y$ buffer layers

Improved device performances compared to CdS reference devices were observed for kesterite-based TFSCs with $Zn_{1-x}Sn_xO_y$ buffer layers deposited by ALD. Primarily, an improved V_{OC} resulting in higher PCE compared to CdS-based devices was achieved [53, 108, 147, 163]. The precise tuning of the band gap and (thus presumably) CB position by varying stoichiometry and deposition temperature during the ALD process of $Zn_{1-x}Sn_xO_y$ [164, 165] was the key factor for excellent device performance. A reduction in interface recombination is ascribed to a favorable CB alignment with the optimized $Zn_{1-x}Sn_xO_y$ buffer layer [166]. Recently, Cui *et al* [53] reported a PCE of 9.3% for CZTS-based TFSCs with ALD-$Zn_{1-x}Sn_xO_y$ buffer layer with an improved V_{OC} (720 mV) as compared to that of the CdS reference cell (PCE = 6.9%, V_{OC} = 652 mV). Similar improvement was also obtained by Li *et al* [108] for CZTSSe-based TFSCs with a PCE of 8.6% as compared to 8.14% PCE for the CdS-buffer device. The highest efficiency using ALD $Zn_{1-x}Sn_xO_y$ buffers for CZTS of 9.7% was reported by Larsen *et al* [118]. In that study, solar cells based on ordered CZTS were compared to devices made from non-ordered CZTS. For non-ordered CZTS the record PCE of 9.7% using ALD-$Zn_{1-x}Sn_xO_y$ was achieved (with ARC). As shown in table 2, the improved PCE originates from improvements in V_{OC}, J_{SC}, and FF. For the cell based on ordered CZTS, a V_{OC} of 809 mV was achieved with the CdS buffer as compared to 778 mV using $Zn_{1-x}Sn_xO_y$. The reason why the use of $Zn_{1-x}Sn_xO_y$ did not result in improved V_{OC} in the ordered case is not clear, but re-optimization of the $Zn_{1-x}Sn_xO_y$ band gap might be needed due to the expected changes in the CZTS absorber upon ordering. The historical PCEs achieved for different kesterite-based TFSCs with Cd-free alternative buffer layers are plotted in figure 5(a), while the *J–V* characteristics in figure 5(b) show the Cd-free record device with a PCE of 9.7% using a $Zn_{1-x}Sn_xO_y$ buffer layer.

3.3.3. In_2S_3-based buffer layers

In_2S_3 is one of the most studied alternative buffer layers for different kesterite-based TFSCs [167, 168, 170, 171]. Among various crystalline forms, the β-In_2S_3 phase has a defective spinel structure that leads to a better stability and optoelectronic properties, in addition to a suitable interface formation with several emerging absorber materials [167, 172]. CBD-In_2S_3 was applied as buffer in CZTSSe-based devices giving efficiencies very close to that of the CdS [107] as seen in table 2. Other successful examples of CBD-In_2S_3 were reported by Jiang *et al* [116] and Hirio *et al* [114], where annealing after buffer deposition was used to improve cell and submodule

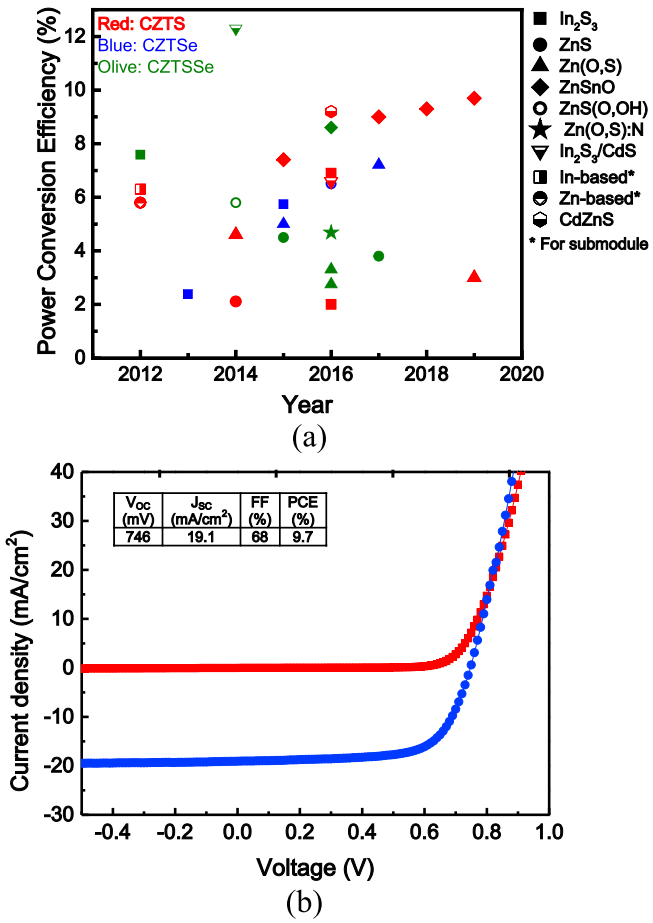

Figure 5. (a) Power conversion efficiencies achieved with several Cd-free alternative buffer layers for different kesterite-based TFSCs; CZTS [53, 114–118, 147, 167, 155–157, 166], CZTSe [112, 113, 168, 158, 169], and CZTSSe [105–108, 158, 153, 154, 159]. (b) *J–V* characteristics of the champion Cd-free CZTS/$Zn_{1-x}Sn_xO_y$ TFSC with ARC.

performance, respectively. Furthermore, a CZTSe device with In_2S_3 buffer layer deposited by spray pyrolysis reaching a maximum PCE of 5.7% was reported [113], but no CdS reference cell performance was stated.

3.4. Metastability related to the front contact

The characteristics of the window layer and the interface it forms with the buffer is also of high importance for the optoelectronic behavior of the device. Indeed, at the buffer/window heterointerface crystalline defects are unavoidably formed that vary in density, charge, and energy position relative to band edges of the buffer material and are likely to induce so-called electro-optical metastabilities. These metastabilities are due to light-dependent (wavelength/intensity) electronic transport, which results in *J–V* curve distortions compared to theoretically expected characteristics. According to Neuschitzer *et al* [173], the electro-optical metastabilities observed in CZTSe/CBD-CdS based devices are caused by negatively charged Cd-vacancies in the CBD-CdS buffer layer. In darkness, these compensating defects are assumed to induce an additional barrier for carriers at the CZTSe/CdS interface, which results in increased R_S values. When such a device is illuminated with low energy photons (i.e. not enough to photo-excite CdS), the observed distortion in the *J–V* curve is called a 'red-kink', and results from blocking of the photo-generated electrons from the absorber. One should notice that this phenomenon was first observed in chalcopyrite/CdS-based devices and ascribed to be due to a too low doped buffer layer [174]. This electron blocking phenomenon is strongly reduced when the CZTSe/CdS device is illuminated with white light (i.e. containing photons of energy higher than 2.4 eV): then, the *J–V* curve appears to be much closer to what is theoretically expected. A possible explanation is that most of the acceptor-like Cd vacancies are neutralized by the photo-generated holes in the buffer. Such wavelength-dependent electronic transport is reversible, meaning that when the device remains in darkness for some time, Cd vacancies turn into negatively charged defects again. Since such metastable defects are strongly influencing the device operation, and thereby the photovoltaic parameters of the solar cells, the community has defined parameters enabling a qualitative estimation of these defects; the most commonly used is the so-called *J–V* cross over. To minimize these metastabilities, many studies are devoted to the formation of interfaces and/or buffer layers free of compensating defects. The CdS buffer

layer is generally prepared by CBD, resulting in a very defective material including significant amounts of O, OH, and other impurities such as C, or N [175]. The actual composition, crystal structure, and morphology and hence the optoelectronic properties of the buffer that ultimately result in the metastabilities described above depend on many experimental parameters (e.g. bath temperature, choice of chemical precursor, …). In order to optimize cell performances and control those metastabilities, Neuschitzer *et al* [173] compared CdS prepared from different Cd precursors. The use of Cd nitrate instead of Cd sulfate results in slower growth kinetics, S-rich composition and suppressed metastabilities. Choubrac *et al* [176] studied the impact of bath temperature and deposition duration on CdS growth mechanism on Ge-kesterite absorbers. The main observation is that—consistent with studies performed on different substrates [177, 178]—after an initial induction/coalescence step, two different growth mechanisms are in competition, namely the ion–ion growth and the cluster deposition. While ion–ion growth results in stable (or non-metastable) solar cells, significant red-kink and crossover phenomena are observed concomitantly in the *J–V* curves of cells for which the buffer was grown in the cluster deposition regime.

Electro-optical metastabilities are not observed exclusively in kesterite cells buffered with CBD-CdS. Indeed, when applying Zn(O, S, OH) buffer layers, Grenet *et al* [105] observed almost no photovoltaic effect before light soaking (LS) but final efficiencies of 5.8% after LS of tens of hours were reached (compared to a PCE of 7.0% for the CBD-CdS buffer reference). They attributed this strong metastability to the presence of an electron barrier at the CZTSSe/Zn(O, S, OH) interface. They further proposed that the LS lowers but does not completely suppress this barrier, which explains the limited performance compared to the CdS reference. Following those observations, Neuschitzer *et al* [173] tuned the anionic content of the Zn(O, S, OH) buffer and showed that a reduction of the S-content in the buffer suppresses metastabilites after LS. Interestingly, they nonetheless achieved the highest efficiencies after LS for cells (based on absorbers with high S-content) exhibiting significant metastabilities. This points to the presence of photoactive defects (likely negatively charged acceptor-like states related to S) in the Zn(O, S, OH) buffer.

4. Summary and conclusions

The contacts used in state-of-the-art kesterite solar cells are still very similar to those used for the more mature CIGSe TFSC technology; Mo back contact and CdS/ZnO/ITO or ZnO:Al front window layer stack. Looking in detail, however, several unique features can be observed for kesterite-based devices. One is the high chalcogen pressure needed during the formation of CZTSSe, causing extensive formation of $Mo(S, Se)_2$ unless barrier (inter)layers are employed. Nevertheless, cells exhibiting thick $Mo(S, Se)_2$ layers do reach the highest efficiencies reported for kesterite-based TFSCs. While alternative back contact stacks have shown improved performance in separate studies, these contacts have not yet resulted in record PCE devices. From a chemical point of view, the back contact also influences diffusion of, e.g. sodium from the SLG substrate into the kesterite absorber. The use of interlayers has in some cases resulted in an increased Na transport into CZTSSe, but we note that if this is due to mechanical defects, poorly controlled non-uniformities might arise. In any case, further attention should be paid to this matter to ensure that blocking of the $Mo(S, Se)_2$ formation does not come at the expense of a uniform Na incorporation.

A relatively new topic for kesterite solar cells is transparent back contacts. ITO and FTO as back contacts have been employed and studied and while indium in-diffusion into CZTS was seen for ITO, FTO showed higher stability. Barrier layers such as thin Mo on FTO further improved stability and gave good front illuminated solar cells.

For the front contact, we have pointed out that record devices for CZTSSe, CZTSe, and CZTS employed a CdS/ZnO/ITO emitter with reduced thickness as compared to most reports. For CZTS, a heterojunction anneal after CdS deposition is important in achieving the highest efficiency, promoting interdiffusion across the heterojunction and apparently transforming the CdS buffer into a $Cd_{1-x}Zn_xS$-based layer in some cases. A review of published data on energy-level alignment at the CZTSSe/CdS interface shows that a beneficial alignment is expected for intermediate and low S contents of the absorber, while for higher S contents, a limiting cliff-like alignment is expected. This result indicates that CdS is a suitable buffer layer if employed on CZTSSe absorbers of that composition range, while other buffer layer materials might be required for S-rich absorbers.

Regarding alternative buffer layer materials, In_2S_3, ZnS-based, and $Zn_{1-x}Sn_xO_y$-based materials are the most studied. Only for $Zn_{1-x}Sn_xO_y$ has superior CZTS-based device performance compared to CdS been reported. For In_2S_3- and ZnS-based buffer layers, relatively high device efficiencies have been shown, but only approaching and not exceeding the PCE of respective CdS reference cells.

Etching and annealing treatments are often an important part of front contact formation. Several different etchants such as KCN and aqueous ammonia are used to remove secondary phases, oxides, and/or sodium compounds from the kesterite surface. A combination of etching and annealing treatments are used in several

cases to reach highest device performance. The annealing can have several roles such as oxidation of GB (if performed in air), redistribution of alkali elements and inducing interdiffusion across the heterojunction, if performed after buffer layer deposition.

Finally, while CZTSSe devices in general are stable, metastable behavior is seen in particular for certain buffer layer materials or processes. Tuning of buffer layer deposition process parameters was shown to minimize this behavior in some cases.

Within the area of front and back contacts for kesterite TFSCs, several open questions remain. At the back contact, the energy level alignment is to a large extent unexplored. Since electrical properties of the $Mo(S, Se)_2$ layer depends strongly on orientation and possible extrinsic dopants that could arise from interdiffusion during absorber formation, studies of the energy level alignment of 'real-world' back contact/kesterite interfaces are crucially required for a detailed understanding and knowledge-based optimization.

Transparent back contacts are another area for which few studies have been reported so far. For this, and the application of barrier (inter)layers on the Mo back contact (to control the $Mo(S, Se)_2$ thickness), the development of methods that guarantee a uniform supply of sodium also needs further attention. For the front contact, a better understanding of the interface formation after heterojunction annealing treatments is needed, including their impact on energy level alignment. Comparative studies of different front contact stacks such as ITO, ZnO:Al, and combinations with or without i-ZnO, $Zn_{1-x}Mg_xO$ or other highly resistive layers are also scarce. For Cd-free buffer layers, $Zn_{1-x}Sn_xO_y$ appears to be most promising, at least for CZTS. More studies are needed to clarify what the optimal $Zn_{1-x}Sn_xO_y$ properties are for a given kesterite absorber deposition process, composition, or degree of order.

In general, as we have shown throughout this review, S- and Se-rich CZTSSe kesterites differ substantially in relation to optimal back- and front contacts. Despite the limited information available about actual $Mo(S, Se)_2$ properties in real devices, the Mo/MoS_2/CZTS contact appears less favorable than for the Se-rich case. For the front contact, different interface annealing treatments are used to optimize CZTS and CZTSe based devices. Furthermore, the energy level alignment at the CZTSSe/CdS interface is only compatible with high PCEs for CZTSSe absorbers with a low to intermediate S-content. Future studies are required to gain further insight into the limiting factors related to the contacts of kesterite TFSC absorbers, in order to pave the way towards further insight-driven advancements.

ORCID iDs

Charlotte Platzer-Björkman https://orcid.org/0000-0002-6554-9673
Marcus Bär https://orcid.org/0000-0001-8581-0691
Jaeyeong Heo https://orcid.org/0000-0002-2602-6538
Tomas Kubart https://orcid.org/0000-0003-2679-2387
Soumyadeep Sinha https://orcid.org/0000-0003-4164-6177

References

[1] Ito K and Nakazawa T 1988 *Japan. J. Appl. Phys.* 1 **27** 2094–7
[2] Friedlmeier T M *et al* 1997 *14th European PVSEC*
[3] Seol J-S *et al* 2003 *Sol. Energy Mater. Sol. Cells* **75** 155–62
[4] Katagiri H *et al* 1997 *Sol. Energy Mater. Sol. Cells* **49** 407–14
[5] Barkhouse D *et al* 2012 *Prog. Photovolt.: Res. Appl.* **20** 6–11
[6] Wang W *et al* 2014 *Adv. Energy Mater.* **4** 1301465
[7] Green M A *et al* 2019 *Prog. Photovolt.* **27** 3–12
[8] Espindola-Rodriguez M *et al* 2017 *ACS Sustain. Chem. Eng.* **5** 11516–24
[9] Becerril-Romero I *et al* 2018 *Prog. Photovolt.* **26** 55–68
[10] Todorov T *et al* 2015 *2015 IEEE 42nd Photovoltaic Specialist Conf*
[11] Suvanam S S *et al* 2018 *Sol. Energy Mater. Sol. Cells* **185** 16–20
[12] Neubauer C *et al* 2019 *Thin Solid Films* **669** 595–9
[13] Antunez P D *et al* 2017 *Adv. Energy Mater.* **7** 1602585
[14] Antunez P D *et al* 2018 *Appl. Phys. Lett.* **113** 033903
[15] Altamura G *et al* 2014 *J. Renew. Sustain. Energy* **6** 011401
[16] Schnabel T and Ahlswede E 2017 *Sol. Energy Mater. Sol. Cells* **159** 290–5
[17] Li X C *et al* 2019 *J. Mater. Chem.* A **7** 9948–57
[18] Haass S G *et al* 2015 *Adv. Energy Mater.* **5** 1500712
[19] Giraldo S *et al* 2018 *Energy Environ. Sci.* **11** 582–93
[20] Lee Y S *et al* 2015 *Adv. Energy Mater.* **5** 1401372
[21] Taskesen T *et al* 2018 *Adv. Energy Mater.* **8** 1703295
[22] Oueslati S *et al* 2015 *J. Phys. D: Appl. Phys.* **48** 035103
[23] Lopez-Marino S *et al* 2016 *Nano Energy* **26** 708–21
[24] Kim J S, Kang J K and Hwang D K 2016 *APL Mater.* **4** 096101

[25] Yan C et al 2018 Nat. Energy 3 764–72
[26] Liu F Y et al 2017 NPG Asia Mater. 9 e401
[27] Liu L S et al 2018 Sol. RRL 2 10
[28] Ge J et al 2016 ChemSusChem 9 2149–58
[29] Chapman B N 1974 J. Vac. Sci. Technol. 11 106–13
[30] Thornton J A and Hoffman D W 1989 Thin Solid Films 171 5–31
[31] Schorr S and Gonzalez-Aviles G 2009 Phys. Status Solidi a 206 1054–8
[32] Paszkowicz W et al 2014 Appl. Phys. A 116 767–80
[33] Malerba C et al 2016 Mater. Des. 108 725–35
[34] Bras P, Sterner J and Platzer-Bjorkman C 2015 J. Vac. Sci. Technol. A 33 061201
[35] Shewmon P (ed) 2016 Diffusion in Solids 2nd edn (Heidelberg: Springer)
[36] Bodegard M et al 1999 Sol. Energy Mater. Sol. Cells 58 199–208
[37] Granath K et al 1997 14th European Photovoltaic Solar Energy Conf. (Barcelona) (Bedford: H S Stephens & Associates)
[38] Gershon T et al 2015 Adv. Energy Mater. 5 1500922
[39] Lopez-Marino S et al 2014 Sol. Energy Mater. Sol. Cells 130 347–53
[40] Salome P M P, Rodriguez-Alvarez H and Sadewasser S 2015 Sol. Energy Mater. Sol. Cells 143 9–20
[41] Sun K W et al 2016 Sol. Energy Mater. Sol. Cells 157 565–71
[42] Scragg J et al 2012 J. Am. Ceram. Soc. 134 19330–3
[43] Gao S S et al 2018 Sol. Energy Mater. Sol. Cells 176 302–9
[44] Abou-Ras D et al 2005 Thin-film compound semiconductor photovoltaics Materials Research Society ed W Shafarman et al (Warrendale, PA: Materials Research Society) pp 287–92
[45] Yang K J et al 2015 Prog. Photovolt. 23 862–73
[46] Li J J et al 2015 Adv. Energy Mater. 5 1402178
[47] Muratore C and Voevodin A A 2009 Thin Solid Films 517 5605–10
[48] Scragg J J S et al 2016 Phys. Status Solidi b 253 247–54
[49] Englund S, Saini N and Platzer-Bjorkman C 2018 Sol. Energy 175 84–93
[50] Scragg J et al 2013 Chem. Mater. 25 3162–71
[51] Shin B et al 2012 Appl. Phys. Lett. 101 053903
[52] Tong Z F et al 2016 Sol. Energy Mater. Sol. Cells 144 537–43
[53] Cui X et al 2018 Chem. Mater. 30 7860–71
[54] Zhou F Z et al 2015 ACS Appl. Mater. Interfaces 7 22868–73
[55] Liu F Y et al 2014 Appl. Phys. Lett. 104 051105
[56] Liu X L et al 2014 Phys. Status Solidi 8 966–70
[57] Lopez-Marino S et al 2013 J. Mater. Chem. A 1 8338–43
[58] Altamura G, Wang M Q and Choy K L 2015 Thin Solid Films 597 19–24
[59] Colina M et al 2016 IEEE J. Photovolt. 6 1327–32
[60] Ranjbar S et al 2016 Phys. Status Solidi a 214 1600534
[61] Nicolet M A 1978 Thin Solid Films 52 415–43
[62] Sharma S 2016 Ultrathin diffusion barrier layers for copper metallization in silicon based integrated circuits Department of Electronic Science Kurukshetra University: Kurukshetra, India
[63] Englund S et al 2018 Phys. Status Solidi a 215 1800491
[64] Shin B et al 2013 Prog. Photovolt. 21 72–6
[65] Englund S et al 2017 Thin Solid Films 639 91–7
[66] Grenet L et al 2018 ACS Appl. Energy Mater. 1 2103–23
[67] Wu W et al 2014 J. Mater. Chem. C 2 3777–81
[68] Cozza D et al 2016 IEEE J. Photovolt. 6 1292–7
[69] Brammertz G et al 2015 IEEE J. Photovolt. 5 649–55
[70] Gunawan O et al 2012 Appl. Phys. Lett. 100 253905
[71] Gunawan O, Gokmen T and Mitzi D B 2014 J. Appl. Phys. 116 084504
[72] Hu S Y et al 2007 J. Alloys Compd. 442 249–51
[73] Kautek W 1982 J. Phys. C: Solid State Phys. 15 L519–25
[74] Kam K K and Parkinson B A 1982 J. Phys. Chem. 86 463–7
[75] Mirhosseini H et al 2016 Thin Solid Films 606 143–7
[76] Yoon J H et al 2014 Prog. Photovolt. 22 90–6
[77] Klinkert T et al 2016 J. Chem. Phys. 145 154702
[78] Malerba C, Valentini M and Mittiga A 2017 Sol. RRL 1 1700101
[79] Agarwal M K, Patel P D and Vijayan O 1983 Phys. Status Solidi a 78 133–6
[80] Sardashti K et al 2017 ACS Appl. Mater. Interfaces 9 17025–34
[81] Dhakal T et al 2015 IEEE 42nd Photov. Specialists Conf. (PVSC)
[82] Bär M et al 2008 Appl. Phys. Lett. 93 042110
[83] Komsa H P and Krasheninnikov A V 2015 Phys. Rev. B 91 125304
[84] Brown C R et al 2019 IEEE J. Photovolt. 9 552–8
[85] Yamaguchi S et al 2015 Japan. J. Appl. Phys. 54 08kc13
[86] Tiong K K et al 1999 J. Cryst. Growth 205 543–7
[87] Molle A et al 2016 Adv. Electron. Mater. 2 1600091
[88] Neal A T, Pachter R and Mou S 2017 Appl. Phys. Lett. 110 193103
[89] Xu E Z et al 2017 Nanoscale 9 3576–84
[90] Nipane A et al 2016 ACS Nano 10 2128–37
[91] Laskar M et al 2014 Appl. Phys. Lett. 104 092104
[92] Spies J A et al 2009 Sol. Energy Mater. Sol. Cells 93 1296–308
[93] Chen S Y et al 2011 Phys. Rev. B 83 125201
[94] Ellmer K 2012 Nat. Photon. 6 808–16
[95] Dixon S C et al 2016 J. Mater. Chem. C 4 6946–61

[96] Keller J et al 2018 Prog. Photovolt. 26 159–70
[97] Minami T 2005 Semicond. Sci. Technol. 20 S35–44
[98] Kykyneshi R, Zeng J and Cann D P 2011 Handbook of Transparent Conductors ed D S Ginley (New York: Springer) pp 171–91
[99] Sarswat P K, Free M L and Tiwari A 2011 Transparent Conducting Oxides and Applications ed J J Berry et al (Cambridge: Cambridge University Press) pp 83–8
[100] Sarswat P K 2012 Alternative methods to fabricate and evaluate copper zinc tin sulfide based absorber layers on transparent conducting electrodes Metallurgical Engineering University of Utah
[101] Ge J et al 2015 ACS Sustain. Chem. Eng. 3 3043–52
[102] Battaglia C et al 2014 IEEE 40th Photovoltaic Specialist Conf. (Pvsc) vol 2014, pp 968–70
[103] Nakada T et al 2004 Sol. Energy 77 739–47
[104] Keller J et al 2018 Prog. Photovolt. 26 846–58
[105] Grenet L et al 2014 Thin Solid Films 564 375–8
[106] Kim J et al 2014 Adv. Mater. 26 7427–31
[107] Barkhouse D A R et al 2012 Appl. Phys. Lett. 100 193904
[108] Li X L et al 2016 Sol. Energy Mater. Sol. Cells 157 101–7
[109] Chone C and Larramona G IMRA Europe
[110] Tampo H et al 2019 ACS Appl. Mater. Interfaces 11 13319–25
[111] Li J J et al 2017 Sol. RRL 1 9
[112] Neuschitzer M et al 2016 J. Phys. D: Appl. Phys. 49 125602
[113] Khadka D B, Kim S and Kim J 2015 J. Phys. Chem. C 119 12226–35
[114] Hiroi H et al 2012 Development of high efficiency CU2ZnSnS$_4$ submodule with Cd-free buffer layer 2012 38th IEEE Photovoltaic Specialists Conf. (New York) (Piscataway, NJ : IEEE) pp 1811–4
[115] Sun K W et al 2016 Adv. Energy Mater. 6 1600046
[116] Jiang F et al 2016 Chem. Mater. 28 3283–91
[117] Yan C et al 2016 Sol. Energy Mater. Sol. Cells 144 700–6
[118] Larsen J et al 2019 Adv. Energy Mater. 9 8
[119] Klein A et al 2010 Materials 3 4892–914
[120] Bär M et al 2011 Appl. Phys. Lett. 99 222105
[121] Bär M et al 2018 ACS Appl. Energy Mater. 1 475–82
[122] Terada N et al 2015 Thin Solid Films 582 166–70
[123] Nagai T et al 2017 Japan. J. Appl. Phys. 56 065701
[124] Bär M unpublished
[125] Yan C et al 2014 Appl. Phys. Lett. 104 173901
[126] Tajima S et al 2013 Appl. Phys. Lett. 103 243906
[127] Li J et al 2013 Surf. Interface Anal. 45 682–4
[128] Bär M, Weinhardt L and Heske C 2016 Advanced Characterisation Techniques for Thin Film Solar Cells ed D Abou-Ras et al (New York: Wiley)
[129] Bär M et al 2011 Phys. Rev. B 84 035308
[130] Bär M et al 2008 Appl. Phys. Lett. 93 244103
[131] Haight R et al 2011 Appl. Phys. Lett. 98 253502
[132] Crovetto A and Hansen O 2017 Sol. Energy Mater. Sol. Cells 169 177–94
[133] Niemegeers A, Burgelman M and Vos A D 1995 Appl. Phys. Lett. 67 843–5
[134] Liu X X and Sites J R 1996 13th Nrel Photovoltaics Program Review ed H S Ullal and C E Witt (New York: AIP) pp 444–52
[135] Minemoto T et al 2001 Sol. Energy Mater. Sol. Cells 67 83–8
[136] Neuschitzer M et al 2015 Chem. Mater. 27 5279–87
[137] Sardashti K et al 2015 Adv. Energy Mater. 5 1402180
[138] Ren Y et al 2016 ACS Appl. Mater. Interfaces 8 18600–7
[139] Bär M et al 2011 Appl. Phys. Lett. 99 152111
[140] Scragg J J S et al 2014 Appl. Phys. Lett. 104 041911
[141] Rey G et al 2014 Appl. Phys. Lett. 105 112106
[142] Valentini M et al 2016 Appl. Phys. Lett. 108 211909
[143] Huang J L et al 2018 Sol. Energy Mater. Sol. Cells 175 71–6
[144] Tajima S et al 2017 Prog. Photovolt. 25 14–22
[145] Hironiwa D et al 2015 Thin Solid Films 582 151–3
[146] Larsen J et al 2017 Thin Solid Films 633 118–21
[147] Ericson T et al 2017 Solar RRL 1 1700001
[148] Xie H B et al 2016 ACS Appl. Mater. Interfaces 8 5017–24
[149] Tajima S et al 2014 Appl. Phys. Lett. 105 093901
[150] Andres C et al 2018 Sol. Energy 175 94–100
[151] Rudmann D et al 2005 J. Appl. Phys. 97 084903
[152] Green M A et al 2019 Prog. Photovolt. 27 565–75
[153] Nguyen M et al 2015 Sol. Energy 111 344–9
[154] Park J Y et al 2017 J. Alloys Compd. 695 2652–60
[155] Kim J et al 2014 Thin Solid Films 566 88–92
[156] Ericson T et al 2014 IEEE J. Photovolt. 4 465–9
[157] Zhang J et al 2019 Thin Solid Films 670 80–5
[158] Li J et al 2017 Solar RRL 1 1700075
[159] Hong H K et al 2016 Sol. Energy Mater. Sol. Cells 155 43–50
[160] Hong H K et al 2017 Sol. Energy 145 20–6
[161] Sinha S et al 2018 Sol. Energy Mater. Sol. Cells 176 49–68
[162] Neuschitzer M et al 2016 J. Phys. D: Appl. Phys. 49 125602
[163] Platzer-Björkman C et al 2015 Appl. Phys. Lett. 107 243904
[164] Kapilashrami M et al 2012 Phys. Chem. Chem. Phys. 14 10154–9

[165] Lindahl J et al 2016 Sol. Energy Mater. Sol. Cells 144 684–90
[166] Platzer-Bjorkman C et al 2015 Appl. Phys. Lett. 107 243904
[167] Siol S et al 2016 ACS Appl. Mater. Interfaces 8 14004–11
[168] Kim S and Kim J 2013 Thin Solid Films 547 178–80
[169] Steirer K X et al 2015 Phys. Chem. Chem. Phys. 17 15355–64
[170] Rajeshmon V G et al 2013 J. Alloys Compd. 553 239–44
[171] Khadka D B, Kim S and Kim J 2015 J. Phys. Chem. C 119 12226–35
[172] Bhira L et al 2000 Phys. Status Solidi a 181 427–35
[173] Neuschitzer M et al 2015 Progress in Photovoltaics 23 1660–7
[174] Gloeckler M, Jenkins C R and Sites J R 2003 Compound semiconductor photovoltaics Materials Research Society ed R Noufi et al (Warrendale, PA: Materials Research Society) pp 231–6
[175] Kylner A, Lindgren J and Stolt L 1996 J. Electrochem. Soc. 143 2662–9
[176] Choubrac L et al 2018 Phys. Status Solidi a 215 1800043
[177] Didden A et al 2011 J. Appl. Phys. 110 033717
[178] Lincot D and Borges R O 1992 J. Electrochem. Soc. 139 1880–9